Available online at www.sciencedirect.com

ScienceDirect

Ceramics International 40 (2014) 901–910

CERAMICS INTERNATIONAL

www.elsevier.com/locate/ceramint

# Phase transitions and structural changes of nanostructured chlorapatite under thermal treatment

Bahman Nasiri-Tabrizi, Abbas Fahami*, Reza Ebrahimi-Kahrizsangi

*Materials Engineering Department, Najafabad Branch, Islamic Azad University, Najafabad, Isfahan, Iran*

Received 30 May 2013; accepted 22 June 2013
Available online 29 June 2013

**Abstract**

The influence of thermal treatment on phase transformations and structural features of mechanosynthesized chlorapatite nanopowders was investigated. Results showed that the phase composition of the product was influenced by the ball to powder weight ratio. During annealing in the range of 900–1300 °C for 1 h, decomposition of chlorapatite to tricalcium phosphate, tetracalcium phosphate, and hydrochloric acid occurred. The rate of decomposition increased gradually with increasing the annealing temperature to 1300 °C. According to the obtained data, during milling process the lattice strain increased significantly to about 1.08%, while the crystalline size declined sharply to around 28.89 nm. After thermal treatment, the crystallite size of chlorapatite went up notably due to a dramatic decrease in residual elastic strain. The crystallinity degree of the 5 h milled sample was about 78.14%. This value reached around 92.86% after annealing at 1300 °C. Scanning electron microscope images indicated that the milled sample had cluster-like structure which was consisted of fine particles with a mean size of about 95 nm. During heating in the range of 900–1100 °C, the coalescence of nanoparticles with spheroidal and polygonal morphologies occurred. After annealing at 1300 °C the microstructure showed a coarse structure characterized by the presence of grains with an average size of around 3 μm.


*Keywords:* Chlorapatite; Mechanochemical; Structural features; Nanopowder; Thermal treatment

## 1. Introduction

Apatites are a group of calcium phosphates that can be represented by the formula $M_{10}(XO_4)_6Y_2$. In this formula, M can be substituted by a large number of various ions like $Ca^{2+}$, $Mg^{2+}$, $Sr^{2+}$, $Ba^{2+}$, $Mn^{2+}$, $Fe^{2+}$, $Zn^{2+}$, $Cd^{2+}$, $Pb^{2+}$, $H^+$, $Na^+$, $K^+$, $Al^{3+}$ and so on. In addition, $XO_4$ can be replaced by $PO_4^{3-}$, $AsO_4^{3-}$, $VO_4^{3-}$, $SO_4^{3-}$, $CO_3^{2-}$, and $SiO_4^{3-}$, while Y can be substituted by several anions like $OH^-$, $F^-$, $Cl^-$, $Br^-$, $O^{2-}$, and $CO_4^{2-}$. Among them, hydroxyapatite (HAp, $Ca_{10}(PO_4)_6(OH)_2$) is one of the most common materials for artificial bone and tooth applications due to its structural and biological properties [1,2]. In addition, synthetic HAp (s-HAp) have been investigated for drug delivery [3], gene therapy [4], chromatography, [5] and waste water remediation [6]. Nevertheless, s-HAp has intrinsically high dissolution rate in a biological system, poor corrosion resistance in an acidic environment, and poor chemical stability at high temperature [7,8].

Many efforts have been made recently to modify the functional specifications of HAp [9–12]. The modification of s-HAp can be accomplished by the substitution of chemical species found in the natural bone [10,11]. These modifications influence the behavior of s-HAp after implantation, namely their chemical and physical properties as well as their bone bonding capability [13]. Although a variety of modified-HAp structures were known, only a limited number of studies have been conducted on the substitution of the chloride ion in the apatite [13,14]. The importance of chloride ions is related to their ability to develop an acidic environment on the surface of bone which resulted in the activation of the osteoclasts in the bone resorption process [15]. According to literature, the substitution of the chloride ion in the apatite was performed by hydrothermal treatments at temperatures in the range of 200–800 °C [16]. In addition, it has been reported that chlorine can be substituted for OH group in the apatite lattice through the wet chemical synthesis. Of course, the extent of chlorine

*Corresponding author. Tel.: +98 3114437009; fax: +98 3312291008.
*E-mail addresses:* ab.fahami@gmail.com, a.fahami@hotmail.com (A. Fahami).

0272-8842/$ - see front matter © 2013 Elsevier Ltd and Techna Group S.r.l. All rights reserved.
http://dx.doi.org/10.1016/j.ceramint.2013.06.085

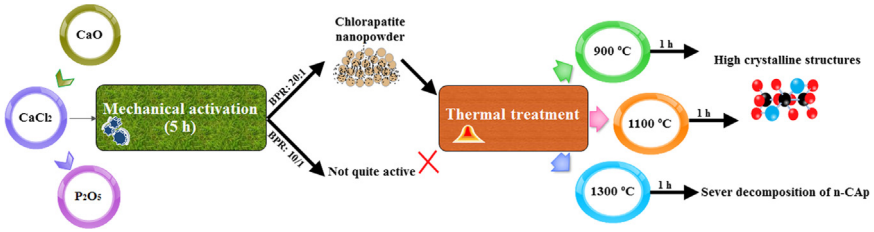


Fig. 1. A schematic view of the whole solid-sate process to synthesize n-CAp.

incorporation depends on the concentration of the precursors [13]. Recently, numerous attempts have been made to develop nanostructured materials by solid-state processes which include mechanical activation (to obtain nanopowders) and subsequent thermal treatment (for recovery of crystallinity degree) [17–19]. High efficiency of this method proposes an appropriate approach to produce commercial amount of nanopowders. However, synthesis and characterization of chlorapatite nanopowders (n-CAp) via a facile solid-state process has not been reported yet.

In the present study, the effect of subsequent annealing on phase transformations and structural features of mechano-synthesized n-CAp was investigated. Moreover, the influence of ball-to-powder ratio (BPR) on phase evolution was examined. The crystallite size, lattice strain, crystallinity degree, lattice parameters, and morphological characteristics of n-CAp were determined and compared in order to propose a suitable conditions for the large scale synthesis of n-CAp.

## 2. Materials and methods

### 2.1. Preparation of n-CAp

The raw materials were of commercial grade calcium oxide (CaO, Merck), calcium chloride ($CaCl_2$, Merck), and phosphorous pentoxide ($P_2O_5$, Merck). A schematic view of the whole solid-sate process to synthesize n-CAp is shown in Fig. 1. The mole ratio of calcium to phosphorous was in accordance with the stoichiometric Ca/P content in the composition of chlorapatite which was equal to 1.67. Mechanical activation was performed in a high energy planetary ball mill at rotational speed of 600 rpm and BPRs of 10:1 and 20:1 under ambient air atmosphere. Polyamide-6 vials (vol. 125 ml) and Zirconia balls (20 mm in diameter) were employed with powder loads of 6 g. Milling was carried out at room temperature without using any process control agent (PCA). To synthesize n-CAp, the mixture of CaO, $CaCl_2$, and $P_2O_5$ was mechanically treated for 5 h according to the following reaction.

$$9CaO+CaCl_2+3P_2O_5 \rightarrow Ca_{10}(PO_4)_6Cl_2 \quad (1)$$

At each sampling, the vial was completely emptied and refilled with new powder charges. After the milling process, the synthesized powder was filled in a quartz boat and then heat-treated in the range of 900–1300 °C for 1 h. It should be noted that the subsequent heating rate from room temperature to the desired temperature was fixed at 10 °C $min^{-1}$.

### 2.2. Characterization of n-CAp

Phase compositions and transformations of the milled sample before and after thermal treatment were examined by X-ray diffraction (Philips X-ray diffractometer (XRD), *Cu-$K_\alpha$* radiation, 40 kV, 30 mA and 0.02° $S^{-1}$ step scan). The XRD patterns were collected over the $2\theta$ angular range between 10° and 70° at scan speed of 1° $min^{-1}$. The XRD patterns were compared to standards compiled by the Joint Committee on Powder Diffraction and Standards (JCPDS), which involved card #27-0074 for CAp, #003-1123 for CaO, #011-0232 for $Ca_4P_2O_9$, and #09-0169 for $\beta$-TCP. The crystallite size and lattice strain of the specimens were determined using the Williamson-Hall method. The Williamson-Hall equation is expressed as follows [20]:

$$B\cos\theta = \frac{0.9\lambda}{D} + \eta\sin\theta \quad (I)$$

where $\lambda$, $D$, $\eta$ and $\theta$ are the wavelength of the X-ray used (0.154056 nm), crystallite size, internal micro-strain and the Bragg angle (°), respectively. Note that $B$ in the above equation is the peak width (in radians) after subtracting the peak width due to instrumental broadening from the experimentally recorded profile. Therefore, when $B\cos\theta$ was plotted against $\sin\theta$, straight lines were obtained for samples with the slope as $\eta$ and the intercept as $0.9\lambda/D$.

The crystallinity degree ($X_c$) was estimated for all the samples by taking the sum total of relative intensities of individual characteristic peaks according to the following equation [21]:

$$X_c = \frac{\mathrm{Sum}(I_1 : I_n)_{CAp}}{\mathrm{Sum}(I_1 : I_n)_{Standard}} 100 \quad (II)$$

where $I_1$:$I_n$ is the total of relative intensities of characteristic peaks of CAp for both the synthesized powders and standard.

The relation between lattice spacing ($d$) and lattice parameters ($a$, $b$, and $c$) of CAp is shown as

$$\frac{1}{d^2} = \frac{4}{3}\frac{h^2+hk+k^2}{a^2} + \frac{l^2}{c^2} \quad (III)$$

where $h$, $k$, and $l$ are the Miller indices of the reflection planes [22].

The unit cell volume ($V$) of CAp was determined using the following equation [23]:

$$V = (3a^2c)(\sin 60^\circ) \quad (IV)$$

The functional groups and structural changes of the samples were measured using Fourier transformed infrared (FT-IR) transmission spectroscopy (Perkin Elmer Spectrum 65 FT-IR Spectrometer, USA) in the range 4000–400 $cm^{-1}$ with the resolution of 2 $cm^{-1}$. For this purpose, the crushed samples were diluted 100 fold with KBr powder and the background noise was corrected with pure KBr data. All spectra were recorded at ambient temperature. The morphological features of n-CAp before and after annealing at 1100 °C were studied by SEM (LEO 435VP, LEO Electron Microscopy Ltd, Cambridge, UK). In addition, the edge-mode of SEM images was used to evaluate the volume fraction of grain boundary of the specimens.

## 3. Results and discussion

### 3.1. Phase evolution

Fig. 2 shows the XRD patterns of 5 h milled powders with different BPRs. At the beginning of milling (initial mixture), phosphoric acid was formed immediately upon addition of $P_2O_5$ to the reaction mixture owing to very high hydrophilic nature of $P_2O_5$.

$$P_2O_5 + 9H_2O \rightarrow 6H_3PO_4, \quad \Delta G_{298\ K} = -493.081\ kJ, \quad \Delta H_{298\ K} = -586.317\ kJ \tag{2}$$

On the other hand, CaO is unstable and can be transformed to calcium carbonate ($CaCO_3$) or to calcium hydroxide ($Ca(OH)_2$) during mixing under air atmosphere. Simultaneously, $Ca(OH)_2$ and $CaCO_3$ can react with phosphoric acid which result in the formation of $CaHPO_4$ as an intermediate phase through the following reactions:

$$CaO + H_2O \rightarrow Ca(OH)_2, \quad \Delta G_{298\ K} = -57.804\ kJ, \ \Delta H_{298\ K} = -65.146\ kJ \tag{3}$$

$$CaO + CO_2 \rightarrow CaCO_3, \quad \Delta G_{298\ K} = -130.447\ kJ, \ \Delta H_{298\ K} = -178.175\ kJ \tag{4}$$

$$Ca(OH)_2 + H_3PO_4 \rightarrow CaHPO_4 + 2H_2O, \quad \Delta G_{298K} = -138.252\ kJ, \ \Delta H_{298\ K} = -121.163\ kJ \tag{5}$$

$$CaCO_3 + H_3PO_4 \rightarrow CaHPO_4 + H_2O + CO_2 \quad \Delta G_{298\ K} = -65.609\ kJ, \ \Delta H_{298\ K} = -8.133\ kJ \tag{6}$$

After 5 h of milling with a BPR of 10:1, a number of characteristic peaks corresponding to CaO, $CaCl_2$, $Ca(OH)_2$, and $CaCO_3$ disappeared and several new peaks emerged especially between $2\theta = 31–33^\circ$ which belonged to the stoichiometrically deficient CAp (CDHAp, $Ca_9(HPO_4)(PO_4)_5(OH)_{1-x}Cl_x$). This shows that the mechanochemical reaction was not yet completed under the milling conditions. On the other hand, after 5 h of milling with a BPR of 20:1, the main product of milling was high crystalline CAp with a trace of CaO. The main reason is that the milling energy will rise and a full mechanical activation may happen while the BPR increases

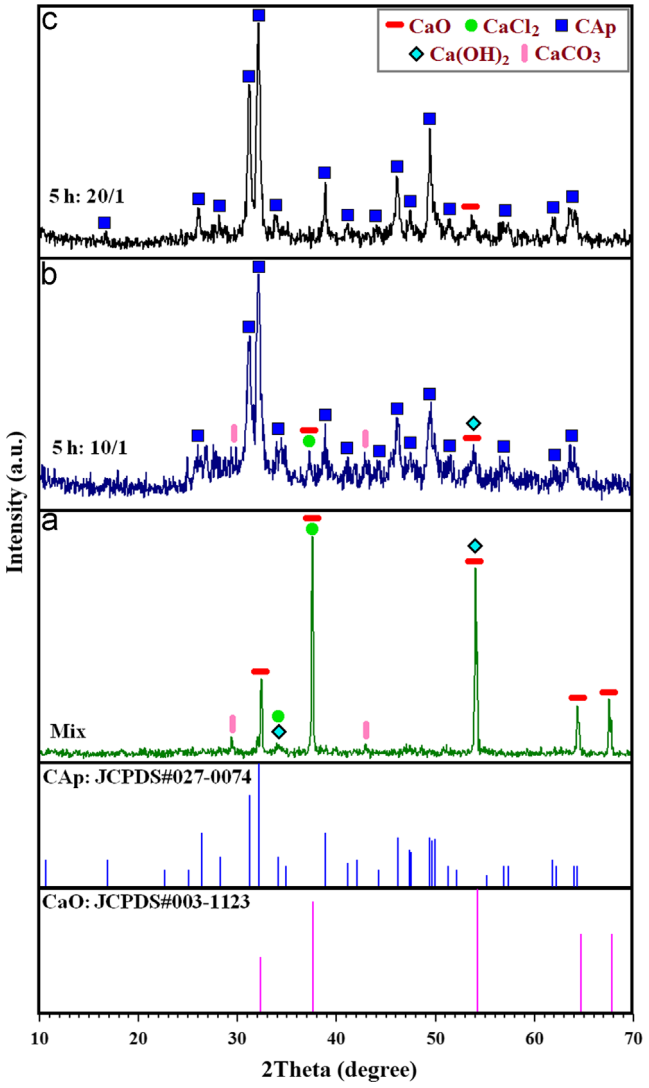


Fig. 2. XRD patterns of 5 h milled powders with different BPRs, (a) mix, (b) 10:1, and (c) 20:1.

to 20:1. It should be noted that the presence of CaO after prolonged ball milling could be a trace of the original product of the original reaction used to produce n-CAp. This result is in good agreement with previous studies [24,25]. Based on XRD profiles, it can be seen that the rate of consumption of raw materials during the milling process was strongly influenced by the ratio of ball-to-powder. By comparing the relative intensities of peaks corresponding to $CaCl_2$ and CaO, it was found that with a BPR of 10:1 the peak intensity of CaO and $CaCl_2$ went down slowly, while those belonging to a BPR of 20:1 almost completely disappeared after 5 h of milling.

Fig. 3 shows the XRD profiles of the 5 h milled sample with a BPR of 20:1 after thermal treatment in the range of 900–1300 °C for 1 h. According to this figure, a noticeable increase in the peaks intensity of CAp was observed. In addition, the breadth of the fundamental diffraction peaks decreased in comparison with the milled specimen which can be attributed to a sharp rise in the crystallite size and a dramatic decline in the lattice strain. It is evident that a slight decomposition of

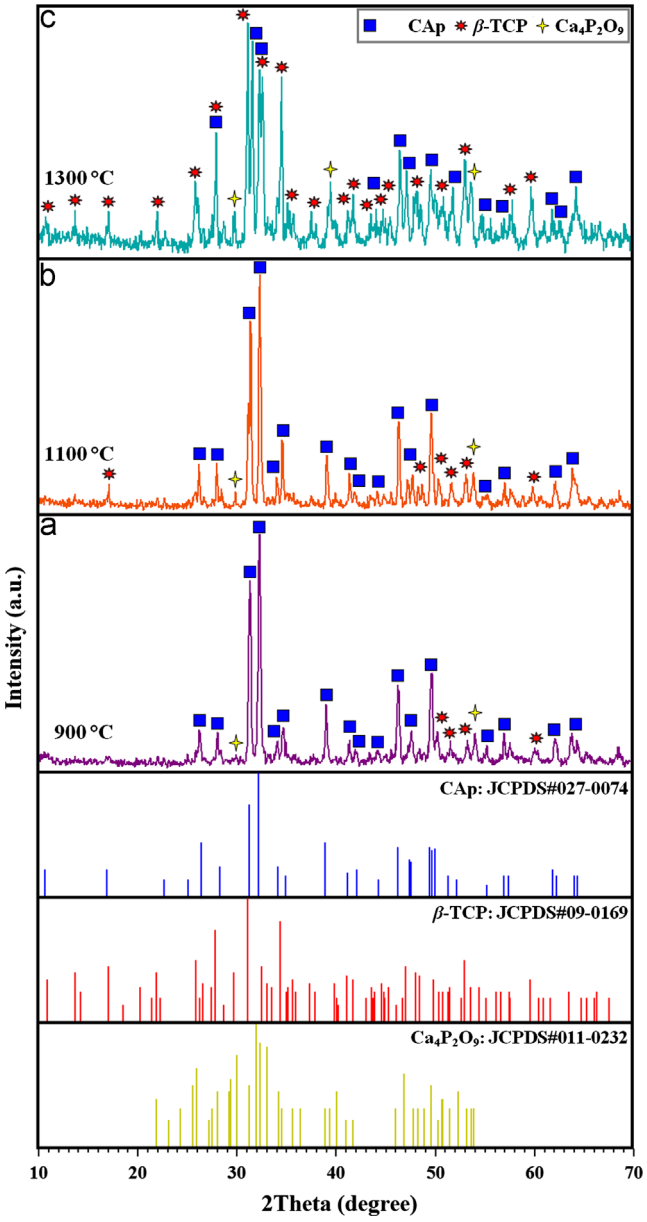


Fig. 3. XRD profiles of the 5 h milled sample with a BPR of 20:1 after thermal treatment, (a) 900, (b) 1100, and (c) 1300 °C for 1 h.

CAp to tricalcium phosphate ($\beta$-TCP), tetracalcium phosphate ($Ca_4P_2O_9$), and hydrochloric acid (HCl) occurred after annealing at 900 °C according to the following reaction:

$$Ca_{10}(PO4)_6Cl_2+H_2O \rightarrow \beta\text{-}Ca_3(PO_4)_2+Ca_4P_2O_9+2HCl \quad (7)$$

In accordance with XRD profiles, the main product of annealing at 900 °C was high crystalline CAp. When the milled sample heat-treated at 1100 °C, similar to previous specimen, high crystalline n-CAp was obtained. With increasing the annealing temperature to 1300 °C, the rate of CAp decomposition increased dramatically and as a result several sharp peaks corresponding to $\beta$-TCP appeared clearly. In this case, the phase compositions were $\beta$-TCP, CAp, and $Ca_4P_2O_9$. It has been found that the final microstructure of TCP will contain $\beta$ or $\alpha$−TCP depending on their cooling rate [26]. Rapid cooling from sintering temperature causes to $\alpha$−TCP phase only, whereas slow furnace cooling leads to $\beta$−TCP phase only. Any moderate cooling rate results mixed phase of both $\beta$ and $\alpha$−TCP. Accordingly, in the present study, the slow furnace cooling rate led to the formation of $\beta$−TCP phase only.

Table 1
Crystallite size and lattice strain of the milled samples before and after annealing.

| Series | Process conditions | $D$ (nm) | $\eta$ (%) |
|---|---|---|---|
| I | BPR: 10/1 | 55.46 | 0.41 |
| II | BPR: 20/1 | 28.89 | 1.08 |
| III | BPR: 20/1+900 °C | 277.30 | 0.05 |
| IV | BPR: 20/1+1100 °C | 346.63 | 0.04 |
| V | BPR: 20/1+1300 °C | 462.17 | 0.01 |

### 3.2. Crystallite size and lattice strain

The crystallite size and lattice strain of the specimens are presented in Table 1. The milled powders with larger lattice strain were obtained after 5 h of milling with BPR 20:1. In addition, higher BPR (20:1) led to the smaller crystallite size. According to the obtained data, the crystallite size of the 5 h milled sample with BPR 10:1 was around 55.46 nm. Higher milling energy in BPR 20:1, led to the full reaction and formation of CAp with the crystallite size of about 28.89 nm. During annealing in the range of 900–1300 °C for 1 h, the residual elastic strain declined sharply that led to a considerable increase in crystallite size. After annealing at 1300 °C, the lattice strain plummeted to about 0.01%, while the crystalline size rose sharply to around 462.17 nm. Therefore, it can be concluded that the crystallite size and induced strain of n-CAp were strongly influenced by the milling and subsequent thermal treatment.

### 3.3. Fraction of crystalline phase (crystallinity degree)

Figs. 4 and 5 show the crystallinity degree ($X_c$) of the milled samples before and after thermal treatment in the range of 900–1300 °C for 1 h. Isolines view of the milled samples with different BPRs is shown in Fig. 4a. These plots display the overlapping range of all scan data in an isolines (contour lines) graph. This view is typically used to show multiple scans as stemming from a non-ambient experiment or a stress measurement [27]. Here, this method was also used to evaluate the fraction of crystalline phase. At early stage of milling (initial mixture), overlapping range of all scan data was very low. In contrast, the 5 h milled sample with a BPR 10:1 showed a modest level of overlapping range of all scan data, specifically in the range of $25° \leq 2\theta \leq 35°$. This behavior is related to the formation of CAp with a moderate degree of crystallinity. In addition, the 5 h milled sample with a BPR 20:1 indicated a low level of extending range of whole scan data which confirmed the formation of high crystalline CAp. In another

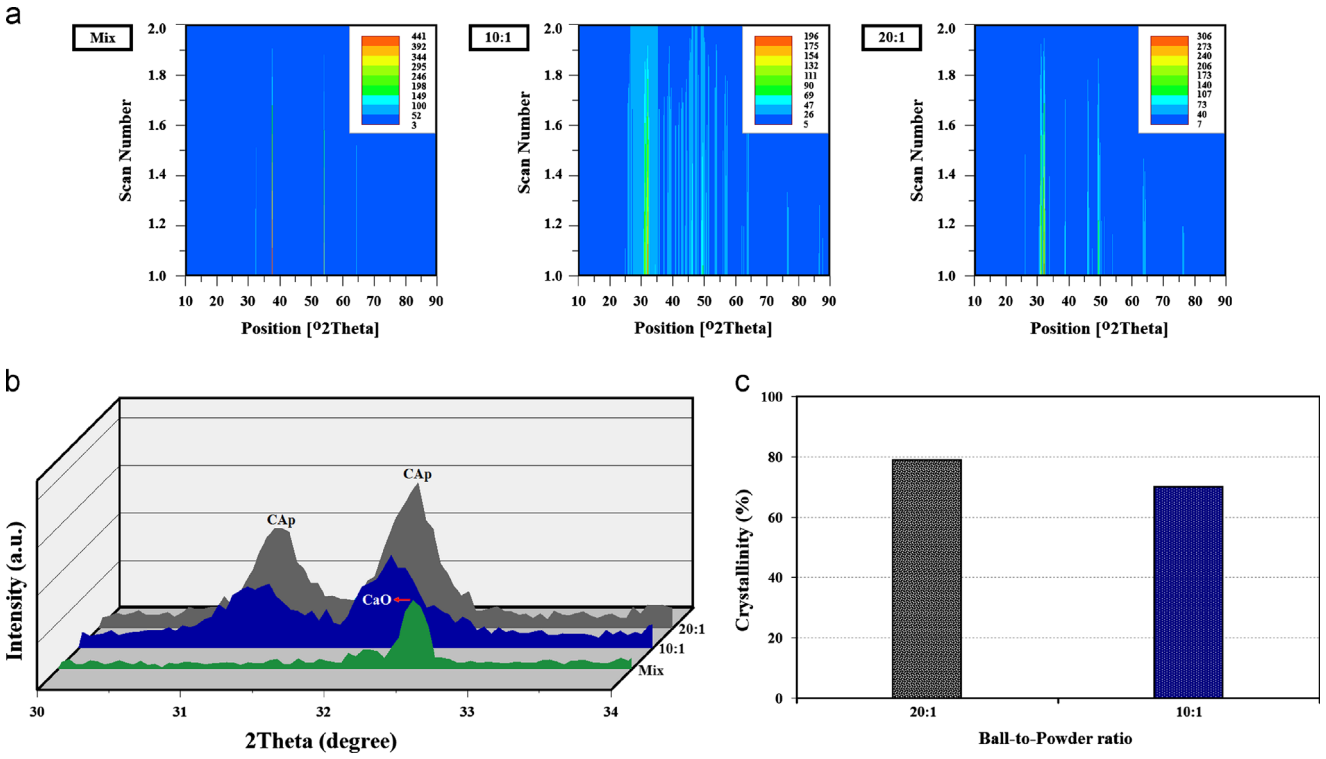


Fig. 4. (a) isolines view, (b) magnified XRD profiles in the range of $30^{\circ} \leq 2\theta \leq 34^{\circ}$, and (c) the crystallinity degree of the milled samples with different BPRs.

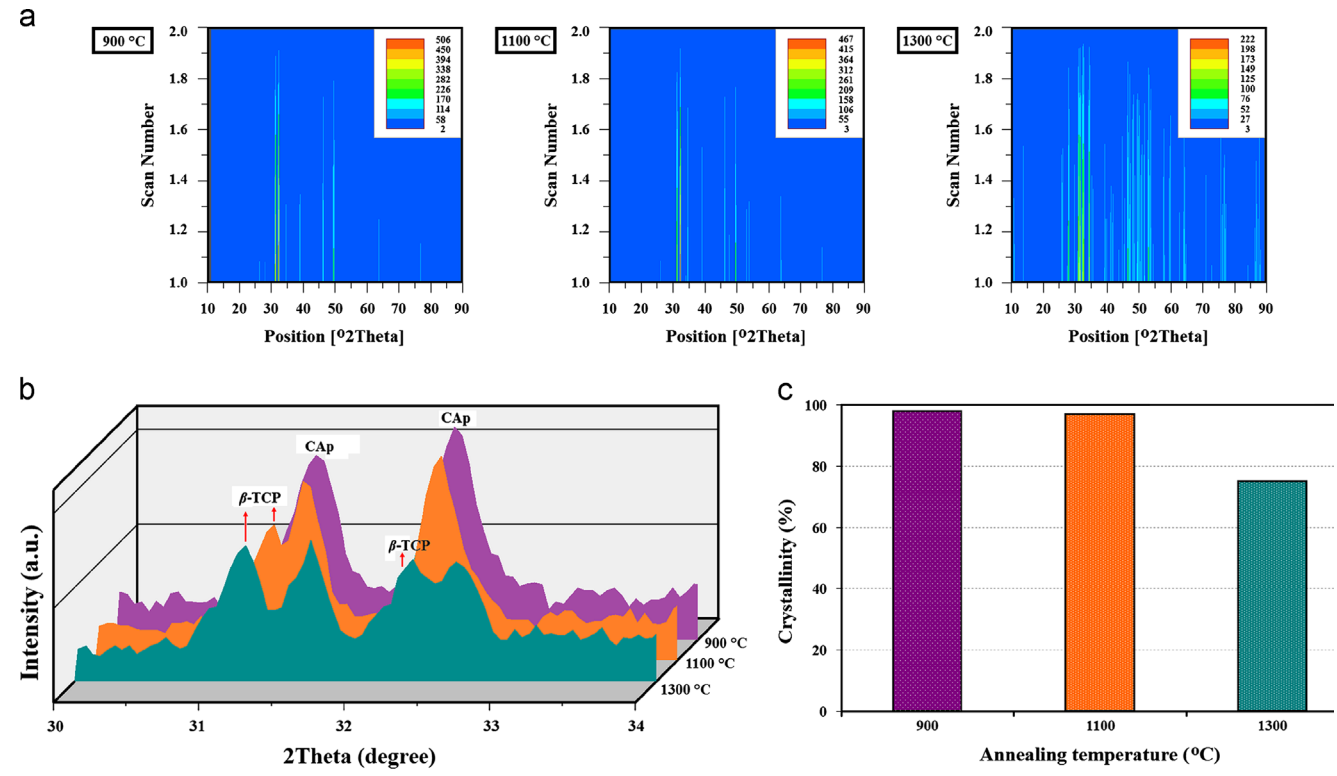


Fig. 5. (a) isolines view, (b) magnified XRD profiles in the range of $30^{\circ} \leq 2\theta \leq 34^{\circ}$, and (c) the crystallinity degree of the milled sample after thermal treatment in the range of 900–1300 °C for 1 h.

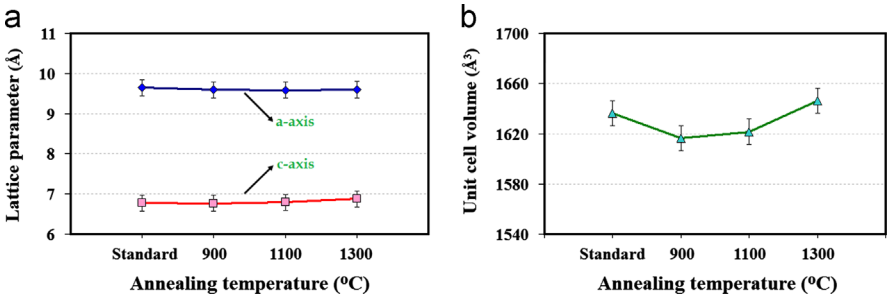


Fig. 6. (a) The lattice parameters and (b) unit cell volume of n-CAp as a function of annealing temperature.

approach (Fig. 4b), the relative intensities of the individual characteristic peaks of the milled sample with a BPR 20:1 was higher than those corresponding to the specimen with a BPR 10:1, remarkably in the range of $30^\circ \leq 2\theta \leq 34^\circ$. This shows that the crystallinity degree of the milled sample with a BPR 20:1 was higher than the milled specimen with a BPR 10:1 as shown in Fig. 4c. These variations in crystallinity degree is justified by milling conditions. As a matter of fact, increased milling energy which achieved by higher BPR and increased speed of rotation, introduces more strain and expands the defect concentration in the powder. This behavior can lead to the amorphization. On the other hand, higher milling energies can also produce more heat, resulting in crystallization of the amorphous phase. A balance between these two effects will determine the nature of the final product phase [20]. Hence, the crystallinity degree of mechanosynthesized CAp was influenced by the milling parameters. In a similar trend, the crystallinity degree of the heat-treated samples was examined (Fig. 5). In accordance with Fig. 5a, overlapping range of all scan data was very low after annealing at 900 and 1100 °C. This indicates that high crystalline n-CAp was produced at these temperatures. On the contrary, the annealed sample at 1300 °C showed a modest level of overlapping range of all scan data, specifically in the range of $25^\circ \leq 2\theta \leq 35^\circ$. This behavior is related to the formation of CAp with a moderate degree of crystallinity. From Fig. 5b, with increasing the annealing temperature the relative intensities of the individual characteristic peaks of CAp decreased especially in the range of $30^\circ \leq 2\theta \leq 34^\circ$ and reached a minimum at 1300 °C. In addition, it is clear that the rate of CAp decomposition increased with increasing the annealing temperature to 1300 °C. As a result, the synthesized nanopowder at 1300 °C showed a minimum crystallinity degree among the heat-treated samples (Fig. 5b). Apatites with high crystallinity degree display little or no activity towards bioresorption and are insoluble in physiological environment [28]. Therefore, the synthesized nanopowders can be considered for biomedical applications.

### 3.4. Lattice parameters and their deviations

Fig. 6 shows the lattice parameters and unit cell volume of n-CAp as a function of annealing temperature. The $a-$axis and $c-$axis values for the milled sample were 9.6250 and 6.8191 Å respectively. These values fluctuated after annealing in the range of 900–1300 °C. According to Fig. 6a, the $a-$axis and $c-$axis values of the heat-treated samples were similar to the reported values for standard (#27-0074: $a=9.6420$ Å and $c=6.7756$ Å respectively). As shown in Fig. 6b, the unit cell volume of CAp declined after annealing at 900 °C. After that, there was a marked upward trend in the value of unit cell volume. It should be mentioned that these variations in the unit cell volume of CAp caused by a rise in the ($a$) parameter, rather than from the ($c$) values and can probably be attributed to the structural evolution of CAp during annealing process. On the whole, in accordance with results, the structural deviations for all the samples were less than 2%.

### 3.5. FT-IR spectra

Fig. 7 displays the FT-IR spectra of the milled sample before and after thermal treatment in the range of 900–1300 °C for 1 h. These spectra reflect the presence of functional groups and structural changes that occurred during milling and annealing processes. In general, the characteristic groups of apatites are $PO_4^{3-}$, $OH^-$, $CO_3^{2-}$, and $HPO_4^{2-}$ groups which commonly appears in 4000–400 $cm^{-1}$ region in the FT-IR spectra [26,29,30]. The characteristic bands of the synthesized nanopowders are as follows:

(a) After 5 h of milling, two bands were detected at 3432.23 and 1642.61 $cm^{-1}$ as a result of the vibration of the adsorbed water in apatites. These bands shifted to 3236.5 and 1684.3 $cm^{-1}$, 3196 and 1684.3 $cm^{-1}$, and 3202.84 and 1684.3 after annealing at 900, 1100, and 1300 °C, respectively. It is obvious that the intensity of these bands declined dramatically after thermal treatment especially at 1300 °C.

(b) In all the samples, the absence of the bands at 630 and 3568 $cm^{-1}$ corresponding to $OH^-$ liberation mode and the appearance of a broad band at 733–758 $cm^{-1}$ confirmed the formation of n-CAp [31].

(c) For the 5 h milled sample, the bands at 1091.7 and 1047.05 $cm^{-1}$ attributed to $\nu_3$ $PO_4$, the band at 960.45 corresponds to $\nu_1$ $PO_4$, the bands at 607.38 and 567.95 $cm^{-1}$ result from $\nu_4$ PO4, and the band at 473.30 $cm^{-1}$ comes from $\nu_2$ vibration of the $PO_4^{3-}$ group [26,30]. These phosphate groups transferred to 1082.6, 1045.39, 960.45, 608.49, 567.94, and 473.74 $cm^{-1}$ for the annealed sample at 900 °C, to 1087.6, 1047.95, 956.18,

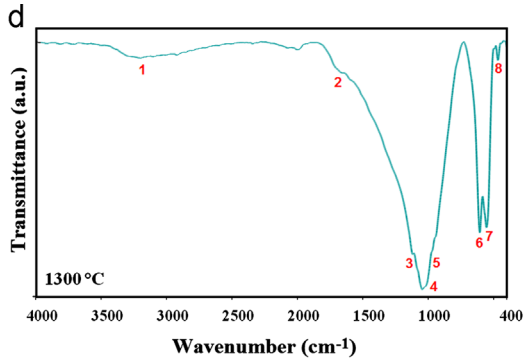


| No. | cm$^{-1}$ | Assignment | No. | cm$^{-1}$ | Assignment |
|---|---|---|---|---|---|
| 1 | 3202.84 | $H_2O$ | 5 | 946.07 | $\nu_1(PO_4^{3-})$ |
| 2 | 1684.3 | $H_2O$ | 6 | 605.60 | $\nu_4(PO_4^{3-})$ |
| 3 | 1113 | $\nu_3(PO_4^{3-})$ | 7 | 553.88 | $\nu_4(PO_4^{3-})$ |
| 4 | 1044.96 | $\nu_3(PO_4^{3-})$ | 8 | 466.66 | $\nu_2(PO_4^{3-})$ |

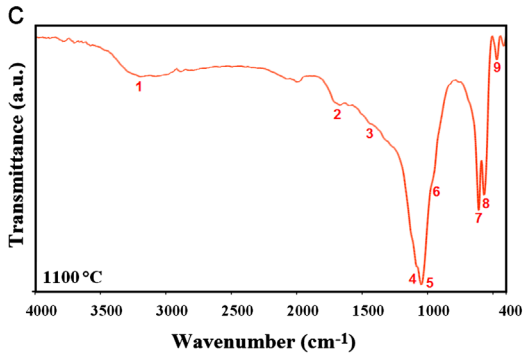


| No. | cm$^{-1}$ | Assignment | No. | cm$^{-1}$ | Assignment |
|---|---|---|---|---|---|
| 1 | 3196 | $H_2O$ | 6 | 956.18 | $\nu_1(PO_4^{3-})$ |
| 2 | 1684.3 | $H_2O$ | 7 | 608.63 | $\nu_4(PO_4^{3-})$ |
| 3 | 1456.7 | $CO_3^{2-}$ | 8 | 567.56 | $\nu_4(PO_4^{3-})$ |
| 4 | 1087.6 | $\nu_3(PO_4^{3-})$ | 9 | 469.93 | $\nu_2(PO_4^{3-})$ |
| 5 | 1047.95 | $\nu_3(PO_4^{3-})$ | | | |

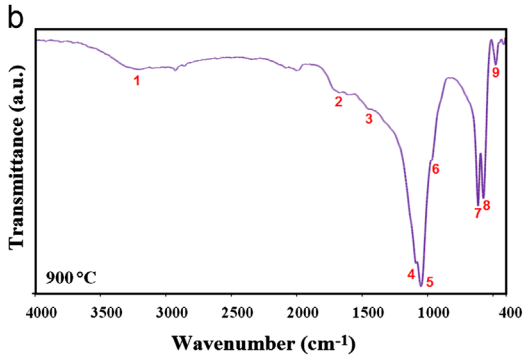


| No. | cm$^{-1}$ | Assignment | No. | cm$^{-1}$ | Assignment |
|---|---|---|---|---|---|
| 1 | 3236.5 | $H_2O$ | 6 | 960.45 | $\nu_1(PO_4^{3-})$ |
| 2 | 1684.3 | $H_2O$ | 7 | 608.49 | $\nu_4(PO_4^{3-})$ |
| 3 | 1456.7 | $CO_3^{2-}$ | 8 | 567.94 | $\nu_4(PO_4^{3-})$ |
| 4 | 1082.6 | $\nu_3(PO_4^{3-})$ | 9 | 473.74 | $\nu_2(PO_4^{3-})$ |
| 5 | 1045.39 | $\nu_3(PO_4^{3-})$ | | | |

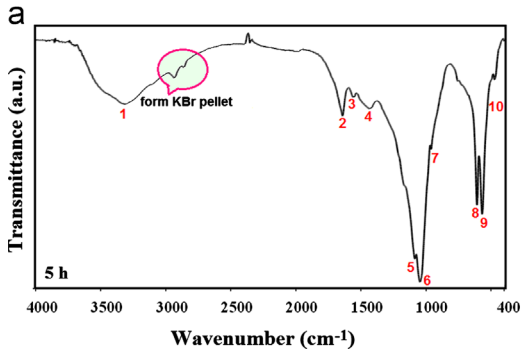


| No. | cm$^{-1}$ | Assignment | No. | cm$^{-1}$ | Assignment |
|---|---|---|---|---|---|
| 1 | 3432.23 | $H_2O$ | 6 | 1047.05 | $\nu_3(PO_4^{3-})$ |
| 2 | 1642.61 | $H_2O$ | 7 | 960.45 | $\nu_1(PO_4^{3-})$ |
| 3 | 1495.7 | $CO_3^{2-}$ | 8 | 607.38 | $\nu_4(PO_4^{3-})$ |
| 4 | 1414.9 | $CO_3^{2-}$ | 9 | 567.95 | $\nu_4(PO_4^{3-})$ |
| 5 | 1091.7 | $\nu_3(PO_4^{3-})$ | 10 | 473.30 | $\nu_2(PO_4^{3-})$ |

Fig. 7. FT-IR spectra of the of the milled sample (a) before and after thermal treatment, (b) 900, (c) 1100, and (d) 1300 °C for 1 h.

608.63, 567.56, and 469.93 cm$^{-1}$ for the heat-treated specimen at 1100 °C, and to 1113, 1044.96, 946.07, 605.60, 553.88, and 466.66 cm$^{-1}$ in the case of the annealed sample at 1300 °C. It is clear that with increasing the annealing temperature to 1300 °C, the $PO_4^{3-}$ vibration peaks at 605.60 cm$^{-1}$ and 553.88 cm$^{-1}$ merged gradually. In addition, the appearance of the band at 1113 cm$^{-1}$ corresponding to the vibration of $PO_4^{3-}$ group in $\beta$–TCP showed a high rate of CAp decomposition after annealing at 1300 °C [32].

(d) For the 5 h milled sample, a doublet appears at 1495.7 and 1414.9 cm$^{-1}$ belonged to $\nu_3$ vibration mode of the carbonated groups. These bands indicates that n-CAp contained some $CO_3^{2-}$ groups in $PO_4^{3-}$ sites of apatite lattice (B-type

substitution) [29]. According to the previous findings, this kind of apatite is more similar to biological apatite and can be very helpful as a bone substitute in orthopedic applications [33]. After thermal treatment at 900 and 1100 °C, the carbonated group was identified by the emergence of a band at 1456.7 $cm^{-1}$. These bands disappeared completely after annealing at 1300 °C.

Based on FT-IR spectra, the high temperature of annealing leads to severe degradation of n-CAp which has adverse effects on product properties.

### 3.6. Morphological features

The morphological features of n-CAp before and after thermal treatment in the range of 900–1300 °C for 1 h are shown in Fig. 8. According to this figure, the synthesized nanopowders had high tendency to agglomerate. It has been found that [34], when two adjacent primary particles collide, the coalescence may take place on the premise that these two particles share a common crystallographic orientation. So, two primary particles attach to each other and combine into a secondary one. Since the sizes of the secondary particles are still very small, it is reasonable that they will continue to collide and coalesce which may ultimately lead to the

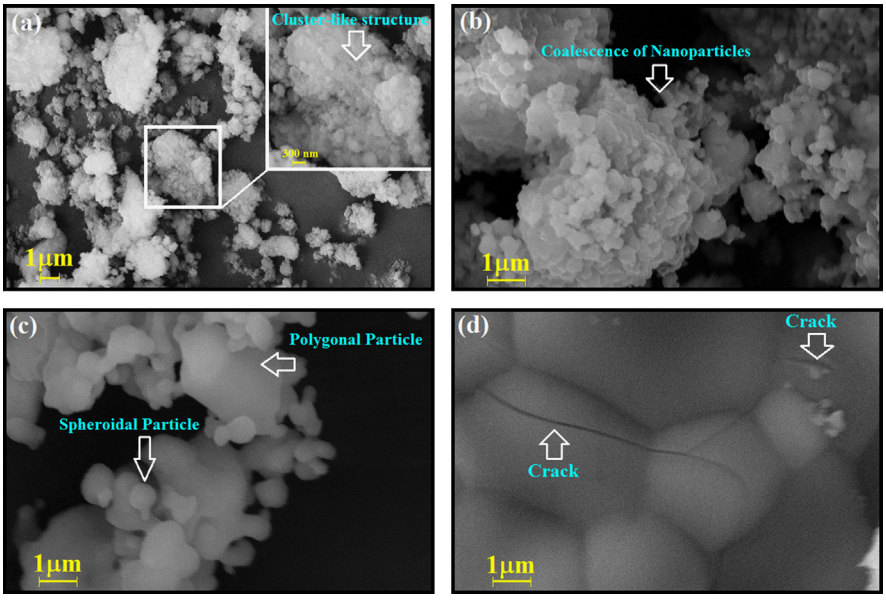


Fig. 8. SEM images of n-CAp (a) before and after thermal treatment, (b) 900, (c) 1100, and (d) 1300 °C for 1 h.

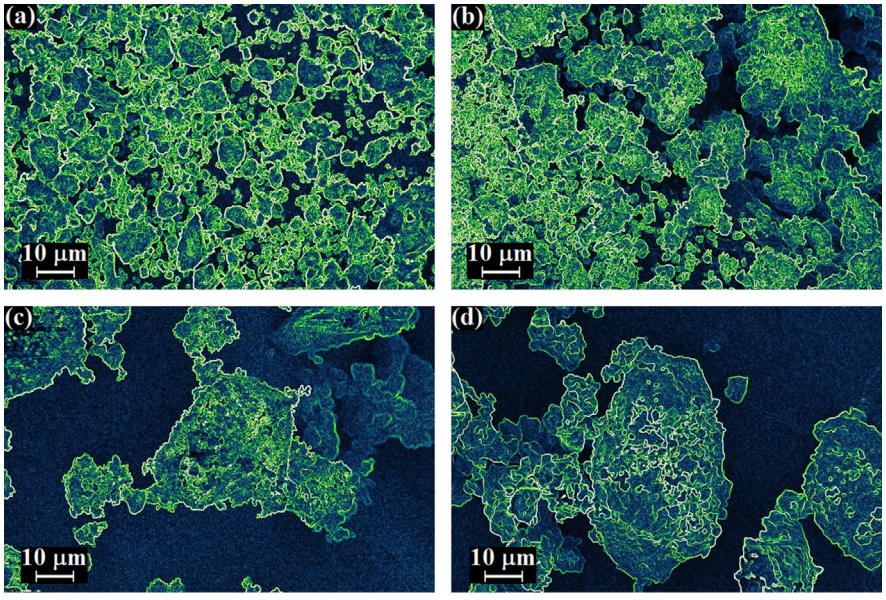


Fig. 9. Edge-mode of SEM images of n-CAp (a) before and after thermal treatment, (b) 900, (c) 1100, and (d) 1300 °C for 1 h.

agglomeration. After 5 h of milling, the particles gradually became equiaxed as shown in Fig. 8a. In this sample, n-CAp showed a cluster-like structure which was composed of several fine particles with an average size of about 95 nm. After thermal treatment, distinct differences in the microstructural characteristics of the specimens became obvious. At 900 °C, the coalescence of nanoparticles was dominant which resulted in the formation of large agglomerates with an average size of about 5 μm (Fig. 8b). When the annealing temperature increased to 1100 °C, grain growth occurred due to a dramatic decrease in residual elastic strain (Fig. 8c). At this temperature, the synthesized powder was comprised of polygonal and spheroidal nanoparticles with an average size of around 350 nm. After annealing at 1300 °C, a pore free/dense microstructure was obtained which was composed of coarse grains with an average size of about 3 μm. According to Fig. 8d, a long crack was formed after thermal treatment at 1300 °C. It is obvious that the crack propagated in a straight path by breaking particles. The main reason is that the internal stress caused by milling accelerated rapid grain growth and resulted in crack formation during thermal treatment [35]. Recalling from the above observations, it can be concluded that the annealing at high temperatures may be associated with abnormal grain growth, which affects the functional specifications of n-CAp.

In the present study, the edge-mode of SEM images was used to evaluate the volume fraction of grain boundary of the nanopowders. Fig. 9 shows the edge-mode images of n-CAp before and after thermal treatment in the range of 900–1300 °C for 1 h. According to this micrographs, the volume fraction of grain boundary in the 5 h milled sample before annealing is higher than the heat-treated specimens. In addition, it is clear that with increasing the annealing temperature to 1300 °C the volume fraction of grain boundary declined dramatically due to the significant growth of agglomerates/nanoparticles. This finding is in good agreement with XRD results in the section of crystallite size and lattice strain. It is obvious that, the synthesized nanopowders before and after annealing at 900 °C had appropriate morphological characteristics that can be very effective in terms of performance.

## 4. Conclusions

The phase transitions and structural changes of mechanosynthesized n-CAp under thermal treatment were investigated. Based on XRD results, the rate of consumption of raw materials during the milling process was strongly influenced by the ball-to-powder ratio. After 5 h of milling with a BPR of 20:1, the main product was high crystalline CAp with a trace of CaO, while with a BPR of 10:1 the mechanochemical reaction was not completed at the same time. Higher milling energy in BPR 20:1, led to the formation of n-CAp with the crystallite size of about 28.89 nm after 5 h of milling. With increasing the annealing temperature to 1300 °C, the rate of CAp decomposition increased dramatically. During annealing at 1300 °C for 1 h, the residual elastic strain declined sharply to around 0.01% which resulted in the formation of coarse structure with a mean crystallite size of around 462.17 nm. After annealing in the range of 900–1100 °C, the synthesized nanopowder showed high crystallinity degree. However, at 1300 °C the fraction of crystalline phase decreased dramatically due to the sever decomposition of n-CAp. According to SEM images, the product was comprised of polygonal and spheroidal nanoparticles with an average size of around 350 nm after annealing at 1100 °C. During heating at 1300 °C, a long crack was formed due to the internal stress caused by the milling process.

## Acknowledgment

The authors are grateful to research affairs of Islamic Azad University, Najafabad Branch for supporting of this research.

## References

[1] M. Okada, T. Furuzono, Hydroxylapatite nanoparticles: fabrication methods and medical applications, Science and Technology of Advanced Materials 13 (2012) 1–14.
[2] S.J. Kalita, A. Bhardwaj, H.A. Bhatt, Nanocrystalline calcium phosphate ceramics in biomedical engineering, Materials Science and Engineering C 27 (2007) 441–449.
[3] Y. Feng, G. Haifeng, Z. Haijiao, H. Xiulan, Polymeric micelle-templated synthesis of hydroxyapatite hollow nanoparticles for a drug delivery system, Acta Biomaterialia 6 (2010) 2212–2218.
[4] I. Ono, T. Yamashita, H.-Y. Jin, Y. Ito, H. Hamada, Y. Akasaka, M. Nakasu, T. Ogawa, K. Jimbow, Combination of porous hydroxyapatite and cationic liposomes as a vector for BMP-2 gene therapy, Biomaterials 25 (2004) 4709–4718.
[5] S.R. Shepard, C. Brickman-Stone, J.L. Schrimsher, G. Koch, Discoloration of ceramic hydroxyapatite used for protein chromatography, Journal of Chromatography A 891 (2000) 93–98.
[6] P. Molle, A. Lienard, A. Gramsik, Apatite as an interesting seed to remove phosphorus from waste-water in constructed wetlands, Water Science and Technology 51 (2005) 193–203.
[7] M. Fini, L. Savarino, N.N. Aldini, L. Martini, G. Giavaresi, G. Rizzi, D. Martini, A. Ruggeri, A. Giunti, R. Giardino, Biomechanical and histomorphometric investigations on two morphologically differing titanium surfaces with and without fluorohydroxyapatite coating: an experimental study in sheep tibiae, Biomaterials 24 (2003) 3183–3192.
[8] Y. Chen, X. Miao, Thermal and chemical stability of fluorohydroxyapatite ceramics with different fluorine contents, Biomaterials 26 (2005) 1205–1210.
[9] G.D. Venkatasubbu, S. Ramasamy, G.S. Avadhani, V. Ramakrishnan, J. Kumar, Surface modification and paclitaxel drug delivery of folic acid modified polyethylene glycol functionalized hydroxyapatite nanoparticles, Powder Technology 235 (2013) 437–442.
[10] A. Zima, Z. Paszkiewicz, D. Siek, J. Czechowska, A. Ślósarczyk, Study on the new bone cement based on calcium sulfate and Mg,$CO_3$ doped hydroxyapatite, Ceramics International 38 (2012) 4935–4942.
[11] Y. Huang, Y. Yan, X. Pang, Electrolytic deposition of fluorine-doped hydroxyapatite/$ZrO_2$ films on titanium for biomedical applications, Ceramics International 39 (2013) 245–253.
[12] P.R. Larson, A.S. Madden, A.C. Tas, Non-stirred synthesis of Na- and Mg-doped, carbonated apatitic calcium phosphate, Ceramics International 39 (2013) 1485–1493.
[13] S. Kannan, J.H.G. Rocha, J.M.F. Ferreira, Synthesis of hydroxychlorapatites solid solutions, Materials Letters 60 (2006) 864–868.
[14] S. Kannan, A. Rebelo, A.F. Lemos, A. Barba, J.M.F. Ferreira, Synthesis and mechanical behaviour of chlorapatite and chlorapatite/β-TCP composites, Journal of the European Ceramic Society 27 (2007) 2287–2294.
[15] P.H. Schlesinger, H.C. Blair, S.L. Teitalbaum, J.C. Edwards, Characterization of the osteoclast ruffled border chloride channel and its role in bone resorption, Journal of Biological Chemistry 272 (1997) 18636–18643.

[16] J.C. Rendón-Angeles, K. Yanagisawa, N. Ishizawa, S. Oishi, Effect of metal ions of chlorapatites on the topotaxial replacement by hydroxyapatite under hydrothermal conditions, Journal of Solid State Chemistry 154 (2000) 569–578.
[17] H. Liu, W. Tang, Y. Wang, C. Liu, G. Xu, Z. Zheng, Structural evolutions of the Fe–40Al–5Cr powders during mechanical alloying and subsequent heat treatment, Journal of Alloys and Compounds 506 (2010) 963–968.
[18] T.F. Marinca, I. Chicinaş, O. Isnard, Structural and magnetic properties of the copper ferrite obtained by reactive milling and heat treatment, Ceramics International 39 (2013) 4179–4186.
[19] C.B. Wei, X.Y. Song, J. Fu, X.M. Liu, Y. Gao, H.B. Wang, S.X. Zhao, Effect of heat-treatment of in-situ synthesized composite powder on properties of sintered cemented carbides, Materials Science and Engineering: A 566 (2013) 96–101.
[20] C. Suryanarayana, Mechanical alloying and milling, Progress in Materials Science 46 (2001) 1–184.
[21] S.S. Rayalu, J.S. Udhoji, S.U. Meshram, R.R. Naidu, S. Devotta, Estimation of crystallinity in flyash-based zeolite-A using XRD and IR spectroscopy, Current Science 89 (2005) 2147–2151.
[22] J. Qian, Y. Kang, W. Zhang, Zh. Li, Fabrication, chemical composition change and phase evolution of biomorphic hydroxyapatite, Journal of Materials Science: Materials in Medicine 19 (2008) 3373–3383.
[23] W.F. Smith, J. Hashemi, Foundations of Materials Science and Engineering. In: Crystal Structures and Crystal Geometry, McGraw-Hill Science, New York, 2004, pp. 67–115.
[24] C.C. Silva, M.A. Valente, M.P.F. Graça, A.S.B. Sombra, Preparation and optical characterization of hydroxyapatite and ceramic systems with titanium and zirconium formed by dry high-energy mechanical alloying, Solid State Sciences 6 (2004) 1365–1374.
[25] B. Nasiri-Tabrizi, A. Fahami, R. Ebrahimi-Kahrizsangi, Effect of milling parameters on the formation of nanocrystalline hydroxyapatite using different raw materials, Ceramics International 39 (2013) 5751–5763.
[26] S. Nath, R. Tripathi, B. Basu, Understanding phase stability, microstructure development and biocompatibility in calcium phosphate–titania composites, synthesized from hydroxyapatite and titanium powder mixture, Materials Science and Engineering C 29 (2009) 97–107.
[27] X'Pert High Score, Version 1.0d, PANalytical B.V., Almelo, The Netherlands, 2003.
[28] M.M. Seckler, M. Danese, S. Derenzo, J.V. Valarelli, M. Giulietti, R. Rodriguez-Clemente, Influence of process conditions on hydroxyapatite crystallinity obtained by direct crystallization, Journal of Materials Research 2 (1999) 59–62.
[29] J.P. Lafon, E. Champion, D. Bernache-Assollant, Processing of AB-type carbonated hydroxyapatite $Ca_{10-x}(PO_4)_{6-x}(CO_3)_x(OH)_{2-x-2y}(CO3)_y$ ceramics with controlled composition, Journal of the European Ceramic Society 28 (2008) 139–147.
[30] R. Ebrahimi-Kahrizsangi, B. Nasiri-Tabrizi, A. Chami, Synthesis and characterization of fluorapatite-titania (FAp–$TiO_2$) nanocomposite via mechanochemical process, Solid State Sciences 12 (2010) 1645–1651.
[31] I. Nikcevic, V. Jokanovic, M. Mitric, Z. Nedic, D. Makovec, D. Uskokovic, Mechanochemical synthesis of nanostructured fluorapatite/fluorhydroxyapatite and carbonated fluorapatite/fluorhydroxyapatite, Journal of Solid State Chemistry 177 (2004) 2565–2574.
[32] I. Cacciotti, A. Bianco, High thermally stable Mg-substituted tricalcium phosphate via precipitation, Ceramics International 37 (2011) 127–137.
[33] M.H. Fathi, E. Mohammadi Zahrani, Mechanical alloying synthesis and bioactivity evaluation of nanocrystalline fluoridated hydroxyapatite, Journal of Crystal Growth 311 (2009) 1392–1403.
[34] A. Fahami, B. Nasiri-Tabrizi, R. Ebrahimi-Kahrizsangi, Synthesis of calcium phosphate-based composite nanopowders by mechanochemical process and subsequent thermal treatment, Ceramics International 38 (2012) 6729–6738.
[35] T. Ryu, K.S. Hwang, Y.J. Choi, H.Y. Sohn, The sintering behavior of nanosized tungsten powder prepared by a plasma process, International Journal of Refractory Metals and Hard Materials 27 (2009) 701–704.